HVI-INDUCED STRESS FIELD: ANALYSIS BY SPH-FEM COUPLED NUMERICAL METHOD

Lorenzo Esposito (1), Tiziana Cardone (2), Sergio Turteltaub (1), Chiara Bisagni (3)

(1) Faculty of Aerospace Engineering, Delft University of Technology, Kluyverweg 1, 2629 HS Delft, the Netherlands
(2) European Space Agency, ESTEC, Keplerlaan 1, 2201AZ Noordwijk, the Netherland
(3) Department of Aerospace Science and Technology, Politecnico di Milano, Via La Masa 34, Milan, 20156, Italy

E-mail: lorenzoexpo21@gmail.com

ABSTRACT

Hyper-velocity impacts from micrometeoroids and orbital debris significantly threaten satellites in low Earth orbit due to high source density and impact frequency. Understanding the stress field around impact points is crucial for satellite design, structural integrity, and platform stability. This study employs a coupled Finite Element Method (FEM) and Smoothed Particle Hydrodynamics (SPH) approach using LS-DYNA software to simulate Hyper-Velocity Impact (HVI) effects on single plate and Whipple shielding system, leveraging the strengths of both methods without compromising result reliability or interface continuity. Unlike previous studies focusing on SPH-FEM coupling, this study characterizes the stress field around the impact zone. Simulations compare results using two contact approaches between SPH and FEM domains: tied and hybrid element contact. Results for the single plate and the Whipple shielding system show the hybrid element contact approach's effectiveness, with stress waves smoothly propagating and minimal reflection at internal methodologies interface.

INTRODUCTION

The near-Earth space has become an invaluable resource for addressing scientific and commercial challenges on Earth. Navigation, Earth observation, remote sensing, and communication are only a few examples of how space has become an integral part of modern life.

However, as our dependence on space technologies increases, so does the quantity of debris orbiting the Earth. They range in size from millimeter aluminum oxide particles to meter-long non-functioning launch vehicle upper stages, posing significant hazards to ongoing missions. According to ESA's space debris environment model MASTER, there are approximately 34,000 debris objects greater than 10 cm in low Earth orbits (LEO), 900,000 objects between 1 cm and 10 cm, and 128 million objects from 1 mm to 1 cm [1]. Therefore, it is highly probable that all spacecrafts will impact with space debris and micro-meteoroids during their operational lifespan.

The term "foreign object damage" is used to describe damage caused by any foreign object or substance to a spacecraft or system in general. This includes impacts from micro-meteoroids and orbital debris (MMOD), which can result in substantial damage that may ultimately lead to mission failure. Such damage can range from localized craterization to subsystem failure or even complete loss of the vehicle.

Hyper-Velocity Impacts (HVI) resulting from collisions at orbital velocities can have significant consequences, occurring at relative velocities higher than 7 km/s. Such impacts can generate a debris cloud, thereby increasing the amount of orbital debris. Potentially, the significant amount of space debris present could result in the "Kessler syndrome", a situation in which the density of objects in LEO due to space pollution is such that collisions between objects could lead to a cascade effect in which each collision creates debris, increasing the likelihood of further collisions [2]. Despite current space policy considering Earth's orbital environment as a finite resource requiring safeguarding and careful planning, the forecast for space debris density is not optimistic [1]. Projections for the next years predict a substantial increase in the number of objects orbiting the Earth. Therefore, it is essential that spacecraft, whether manned or unmanned, are sufficiently shielded against the risk of HVI damage.

Currently, engineering provides both active and passive solutions to address this issue. Active solutions, such as evasive maneuvers, are only applicable to trackable objects. For non-trackable objects with a main dimension less than 5 cm, space engineers must rely on passive systems. Spacecraft shielding systems are effective passive means to protect against MMOD. The most commonly used and reliable solution is the Whipple shield, a dual-wall system proposed in 1947 [3] (Fig. 1).

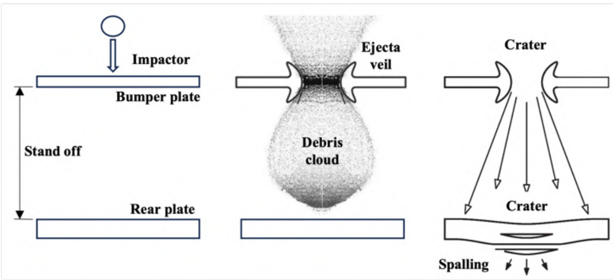

Figure 1: Conventional Whipple shield: (left) initial configuration, (central) post-impact debris cloud generation and (right) impact on rear plate.

The system typically comprises a single thin plate, called bumper, that is positioned at a short distance from the spacecraft's primary structure. Its primary objective is to fragment and/or vaporize the projectile, resulting in the formation of a debris cloud that expands and distributes the energy and the impulse load of the projectile over a larger area onto the rear wall, reducing the degree of damage to the spacecraft's primary structure [4].

With the increasing need for spacecraft stability to ensure the proper operation of increasingly precise instruments, perturbations encountered in orbital conditions, once considered negligible, have now become a problem [5]. MMOD impacts can induce disturbance waves that propagate throughout the spacecraft structure, potentially leading to measurement inaccuracies that prevent successful mission fulfillment. For these reasons, comprehending the development of HVIs in orbit has become a significant concern within the field of space engineering.

Although experimental research is still needed, it can only offer a partial answer to meet the growing demand for more effective design solutions [6]. Furthermore, the intricate experimental procedures and high infrastructure costs make numerical simulation an appealing alternative. Numerical models can guide experimental design and provide solutions for unexplored scenarios that are not achievable in experiments.

Most numerical simulations for such events rely on Smoothed Particle Hydrodynamics (SPH) models [7]. This numerical methodology is most suitable for simulating phenomena characterized by substantial material deformations. On the other hand, the computational cost of such modeling is particularly onerous. Additionally, given the prevalent practice of evaluating satellite structural dynamics using its FE model, a methodology capable of combining the two numerical techniques and exploiting both advantages is sought, guaranteeing accurate results while maintaining a sustainable computational cost. With a coupled approach, it is possible to achieve a higher degree of accuracy in the results and ensure reasonable simulation times by maintaining the use of FEM in regions away from critical areas.

Through LS-DYNA software, two different SPH/FEM interface were implemented to ascertain whether an algorithm performs more effectively than the other: "tied contact" and "adaptive contact". Moreover, the effect of different SPH domain shapes (square and circular) on the propagation of stress from one domain to the other was assessed. The objective was to determine the influence exerted by the interface geometry and interface geometrical discontinuity on proper propagation of information.

SINGLE PLATE

The methodology has been firstly developed for a single plate configuration. To validate and compare the simulation approach, the implemented models replicate the experimental test No. 3 conducted by Sibeaud et al. [8]. The test consisted of a 5 mm radius spherical projectile made of aluminum alloy Al 2017 shot onto a 2 mm thick, 150 mm square plate made of aluminum alloy Al 6061-T6 at normal incidence with a measured velocity of 5941 m/s.

The thermoplastic behavior of the aluminum parts under high strain rates, large deformations and elevated temperatures is modeled using a Johnson-Cook model in combination with a Gruneisen equation of state. Due to limitations in obtaining adequate Johnson-Cook material model data for Al 2017, and noting the similarity in material characteristics, both parts were modeled using data commonly associated with Al 6061-T6 aluminum alloy. It has been demonstrated that for HVIs materials exhibit a hydrodynamic behavior. In this regime, strength properties effects become negligible respect to density [9].

The (initial) elastic behavior of the aluminum parts is characterized with a linearly isotropic model. The elastoplastic model parameters are indicated in Tabs. 1 and 2.

Material Property	**Symbol**	**Value**	
Density	ρ	2.703	g/cm^3
Elastic Modulus	E	69	GPa
Poisson's Ratio	ν	0.33	
Melting Temperature	T_m	775	K
Reference Temperature	T_0	273	K
Specific Heat	c_p	875	J/kgK

Table 1: Material properties of Al 6061-T6 aluminum alloy [10, 12].

Johnson-Cook Parameters	**Symbol**	**Value**	
Yield Stress	σ_y	324.1	MPa
Strain Hardening Param.	B	113.8	MPa
Strain Hardening Exp.	n	0.42	
Strain Rate Param.	C	0.002	
Thermal Softening Exp.	m	1.34	
Pressure Cut-off	σ_p	-1200	MPa
Damage Constant 1	D_1	-0.77	
Damage Constant 2	D_2	1.45	
Damage Constant 3	D_3	0.47	
Damage Constant 4	D_4	0	
Damage Constant 5	D_5	1.6	

Table 2: Johnson-Cook material model parameters for Al 6061-T6 aluminum alloy [11, 12].

The Grüneisen EOS has been implemented using the parameters that are presented in Tab. 3.

Grüneisen parameters	**Symbol**	**Value**	
EOS Constant 0	C	5328	m/s
EOS Constant 1	C_1	1.4	
EOS Constant 2	C_2	0	
EOS Constant 3	C_3	0	
Grüneisen Parameter	Γ_0	1.97	
Factor A	A	0.48	

Table 3: Grüneisen EOS parameters for Al 6061-T6 aluminum alloy [13].

The Johnson-Cook material model and the Grüneisen

EOS were chosen because of their demonstrated accuracy in modeling high-velocity impacts in metals [14, 15]. To evaluate and compare different simulation settings, the following parameters were measured and used as benchmarks, since they were also recorded during the experimental campaign [8]: (i) final crater radius, (ii) debris cloud length, (iii) maximum cloud radius, and (iv) axial velocity at the cloud front 16 µs after impact, which is a representative instant after the perturbation has traveled from the domain modeled with SPH to the domain modeled with FEM.

Quarter Plate

To reduce computational costs, exploiting the model symmetry, only a quarter of the domain is modelled numerically (Fig. 2). Symmetry planes in LS-DYNA are used for solid elements and SPH particles.

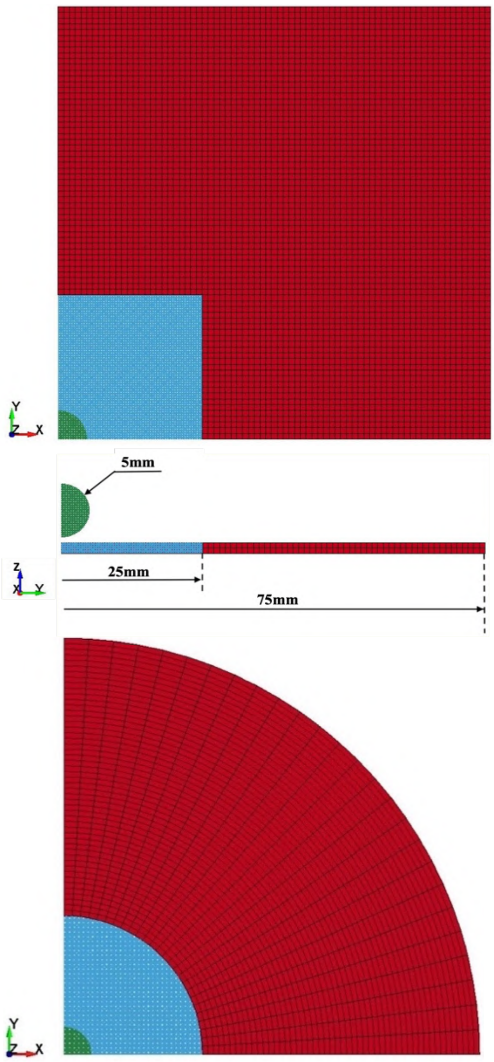

Figure 2: Geometry of the quarter plate model with tied contact (square and circular SPH impact domain).

As the focus is on selecting the optimal SPH domain shape and SPH/FEM interface algorithm that would allow for the most accurate numerical reproduction of HVI in space, both square and circular SPH domain shapes were tested, and two SPH/FEM interface algorithms were evaluated: "tied contact" and "hybrid elements contact". The different test settings are summarized in Tab. 4.

	Tied Contact	**Hybrid Contact**
Square Domain	Square domain with tied contact (Test 1)	Square domain with hybrid contact (Test 3)
Circular Domain	Circular domain with tied contact (Test 2)	Circular domain with hybrid contact (Test 4)

Table 4: Implemented numerical tests.

The tied contact enforces a kinematic constraint at the SPH/FEM interface, thereby ensuring coherent solutions along the boundary. The link between the SPH particles and the segment set of FEs faces that are oriented towards the SPH domain are established enforcing a node-to-surface constraint. This configuration establishes a tied linkage, thereby limiting the translational degrees of freedom of the elements and nodes [16].

The second type of contact methodology involves the creation of a transition zone, with a thickness of 1mm, between the SPH and FEM plate components. This methodology entails the introduction of hybrid solid elements between the SPH and the FE domain of the plate. Each hybrid element employs both solid and particle discretization techniques [16]. The hybrid elements are then constrained through tied contacts to both domains. On the FEs domain side, this is achieved using a surface-to-surface tie constraint, while on the SPH domain side, it is accomplished through the use of the node-to-surface constraint.

Fig. 3 shows a detail of the SPH/FEM hybrid interface method. The hybrid domain, consisting of solid elements and SPH particles, is rendered in yellow. To enhance clarity, the yellow solid elements have been made transparent and some have been blanked out to show the presence of the brown SPH particles in the interior.

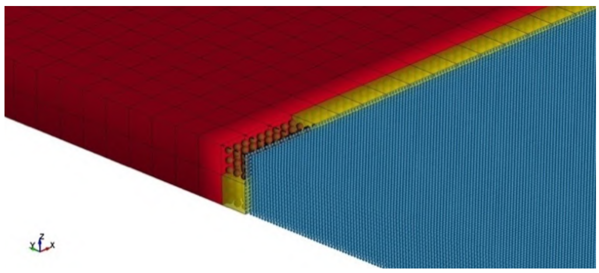

Figure 3: Detail of the hybrid elements contact method between the SPH (in blue) and FEM (in red) domain.

The use of this contact system, which is still based on kinematic constraints, ensures a smoother transition due to the dual nature of the transition area, resulting in more accurate stress propagation. The interaction works by constraining SPH node locations with solid elements, while SPH elements introduce a penalty force term against solid node movement [16].

The function offers flexibility in specifying the number of SPH particles generated per element. Hexahedral elements can contain n^3 SPH elements, where n ranges from 1 to 3. To ensure the accurate establishment of the hybrid contact, the coupling is triggered at the beginning of the simulation. In the transition zone between the SPH and FEM domains, 27 particles per solid element (n = 3) are generated (Fig. 3). This value represents a balanced compromise between computational efficiency and accuracy. It should be noted that the transition zone is placed significantly away from the point of impact, which eliminates the need for a higher particle count.

To validate the simulations, the relative differences between the simulations and the experimental results for the key metrics are listed in Tab. 5.

The results indicate that the circular domain with hybrid contact case (i.e., Test 4) exhibits a slightly better overall match with the experimental results, as illustrated in the final column of the table. The averaged relative differences values in this column are calculated using a weighted average, where a weight of 0.8 is applied to the crater diameter on the plate. This reflects the fact that the crater diameter is considered less critical than the other metrics, which are assigned a unitary weight. The rationale behind this weighting is that the primary concern in HVI scenarios is the debris cloud, making the other metrics more important in assessing overall damage..

However, this difference is not conclusive due to small variations and challenges in precisely defining a boundary when dealing with individual SPH particles. This ambiguity introduces subjectivity into the selection of boundary particles. Based on the data presented, it is clear that the type of SPH/FEM contact setting and the SPH domain shape have only a limited influence on the morphology of the resulting crater and debris cloud.

Stress Analysis in the Plate

The choice of SPH/FEM contact setting mainly affects the propagation of stress waves from the impact site to the rest of the panel. It is important to note that the need to find the best way of coupling between the SPH and FE domains arises from the requirement for accurate propagation of stress wave from the impact site to the satellite in order to evaluate the effect of the MMOD HVI on the new generation of satellites equipped with increasingly sensitive instrumentation.

In order to assess the best configuration for this type of analysis, qualitative and quantitative evaluations have been conducted. Fig. 4 shows the propagation of the stress wave from the impact site to the rest of the plate by varying simulation settings. The results of four successive times SPH/FEM stress-wave transition process (7, 9.5, 12, and 14.5 μs post-impact) are reported.

The images suggest a potential improvement with a circular SPH domain (Test 2 and 4). The stress wave propagates smoother and is not affected by the discontinuity at the methodology interface. However, it is possible that the observed enhancement is primarily due to a uniformity and synchronicity of errors, particularly concerning equidistant points from the impact center.

Thus, in order to appreciate the differences induced by the use of different contact setting, it is interesting to analyze the artificial reflection of stress waves within the plate. It allows to understand if non-physical phenomena can occur at the interface of different modeling methodologies, which may compromise the accuracy of the simulation. The study was performed only on the circular domain configuration for simplicity's sake.

To analyze the effect of the SPH/FEM interface, von Mises stress history data were collected at two adjacent measurement spots across the interface. Stress data concerning the SPH domain is averaged between the stress data curves concerning particles placed within a small box equal in size to a finite element. The approach is based on the assumption that stress data between two adjacent location sections should be congruent over time, despite a temporal displacement proportional to the velocity of the shock wave within the material and a marginal attenuation of the signal amplitude due to inherent damping effects induced by the stiffness of the plate. This congruence should persist even when the measurement points lie across two different numerical methodology domains. Any significant variations in the stress profiles, deviating from the expected congruence, may indicate the presence of reflective phenomena occurring at the interface between these domains.

The von Mises stress curves for the tied and hybrid contact methodology are shown in Fig. 5.

	Crater diameter (final) [mm]		Front cloud velocity (16 μs) [m/s]		Cloud length (16 μs) [mm]		Cloud max. diameter (16 μs) [mm]		|ε avg.|
Exp. data	18.90		5296		81.1		65.6		
Test 1	21.36	(13.02 %)	5241	(-1.04 %)	80.7	(-0.5 %)	67.2	(2.44 %)	**3.60 %**
Test 2	21.37	(13.07 %)	5249	(-0.89 %)	82.2	(1.4 %)	66.3	(1.07 %)	**3.46 %**
Test 3	21.11	(11.69 %)	5298	(0.04 %)	80.4	(-0.9 %)	68.6	(4.57 %)	**3.72 %**
Test 4	21.21	(12.22 %)	5276	(-0.38 %)	80.6	(-0.6 %)	67.6	(3.05 %)	**3.44 %**

Table 5: Results and absolute value of the averaged relative differences between simulation and experimental results of single plate simulations (quarter model).

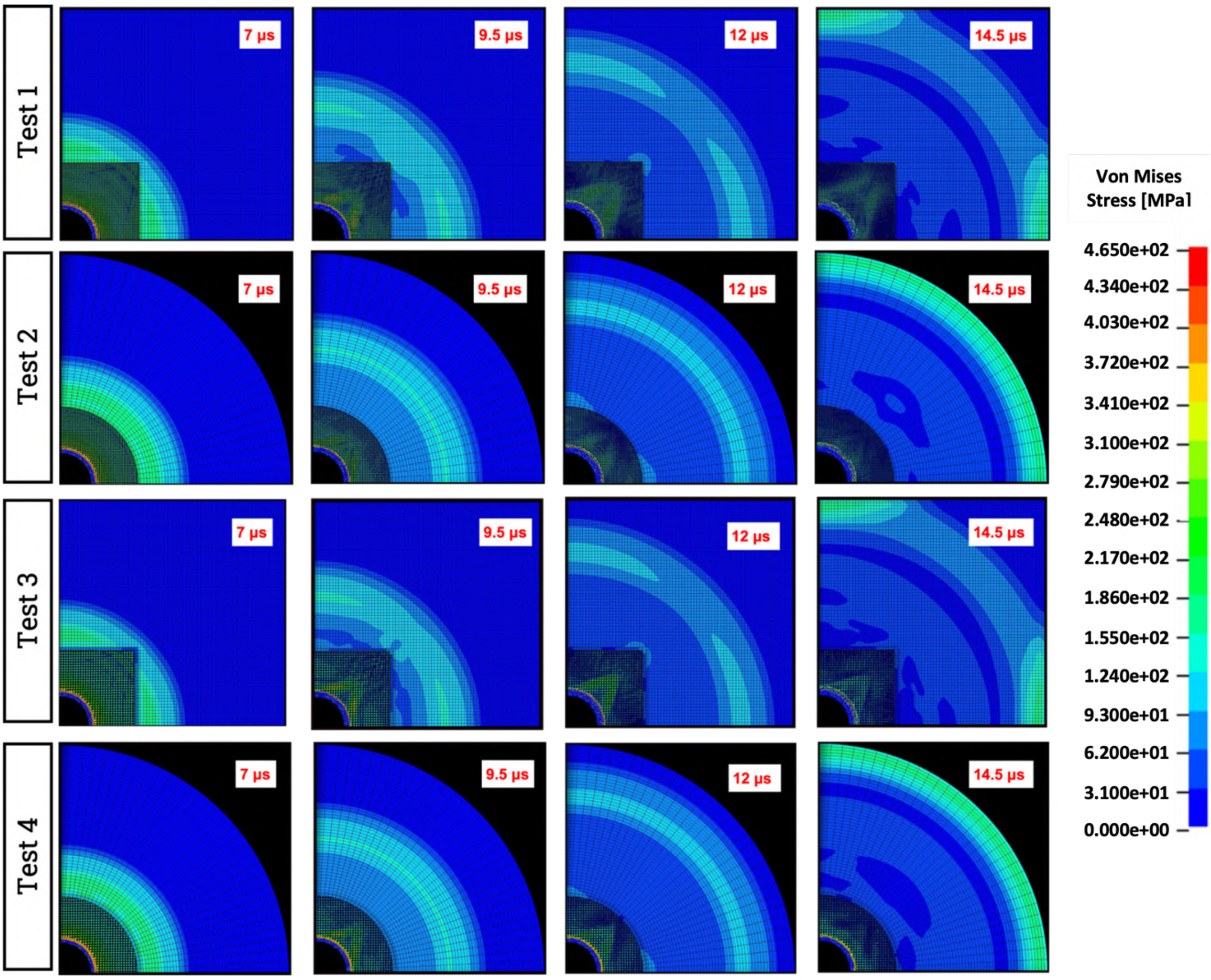

Figure 4: Stress wave propagation in single plate simulations at different timesteps after the impact.

Upon analysis, it is clear that there is a strong correlation between the data collected in the SPH and FEM domains. The results support the hypothesis of a temporal shift and a slight attenuation of the signal amplitude. Indeed, to be comparable with the FEM data curve and to highlight the differences between the two, the signal obtained in the SPH domain has been shifted in time. Both curves show the main stress peaks occurring simultaneously. The peaks are highlighted in the graph with a yellow arrow along a dashed line added to emphasize the temporal fit.

In the graphs, small black circles are used to highlight stress peaks in the SPH data curve (in green) that do not appear in the respective FEM curve (in red). The smaller stress peaks that occur immediately after a larger peak do not have a match in the FEM stress curve. Given the isotropic and homogeneous nature of the model material, these peaks are likely related to a numerical induced error. It is possible that they are related to the reflection of the stress waves in the proximity of the SPH/FEM interface.

By comparing the results from the tied (Test 2) and the hybrid contact (Test 4), it is possible to observe that the latter methodology has a better performance in terms of the amplitude of these reflected peaks. Although the reflected stress peaks present in the tied contact configuration are not entirely eliminated through the use of an adaptive contact, their influence has been significantly mitigated. These findings were interpreted as indicative of reduced reflection of the stress wavefront propagating from the center outward at the interface between the two methods employed.

It is important to note a general trend in the von Mises stress plots showing that, after a certain period of time, as highlighted by the light blue line in Fig. 5, the stress field tends to become more uniform within the impacted plate. Indeed, as the simulation progresses, the SPH and FEM differences in stress tend to diminish. To achieve full uniformity of the stress field, it may be necessary to implement longer simulations and larger plates to avoid boundary reflections.

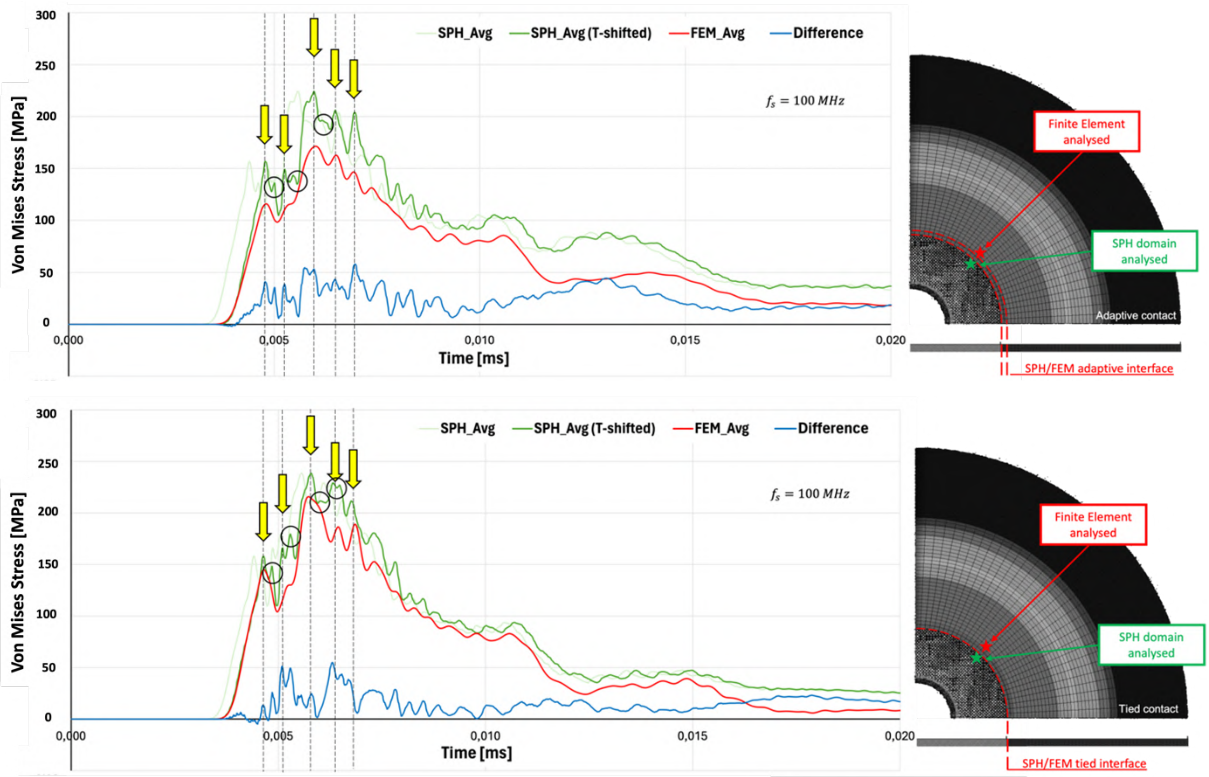

Figure 5: SPH and FEM von Mises stress data comparison in circular Test 2 and 4.

WHIPPLE SHIELD

In this section, the model implemented for the simulation of HVI in a Whipple shield configuration is outlined. The model proposed in the following sections benefits from the comparative studies conducted on the single-plate scenario. Specifically, the configuration with a circular-shaped SPH domain and hybrid SPH/FEM contact algorithm has been shown to provide a high degree of accuracy in simulating the impact dynamics.

To validate the proposed model, the simulation replicates an experimental test conducted at the Ernst Mach Institute in Freiburg, Germany [17]. The experimental data were obtained in the frame of an activity of Airbus Defence and Space under an ESA contract and are courtesy of Airbus Defence and Space.

In the replicated experiment, a 5 mm diameter spherical projectile made of Al 2007 is shot at 7.1 km/s against a perpendicular Whipple shield. The plates of the shield are made of Al 2024-T3 with a thickness of 0.8 mm. They are assumed to be square and, although their dimension is not specified, to minimize boundary conditions interference, both plates were modeled with 300mm long external edges. The distance between the two plates is 60 mm. A schematic illustration of the test set-up is shown in Fig. 6. The model geometry was configured to closely resemble the experimental context. Fig. 7 presents a comprehensive view of the simulated system. The SPH impact zone is shown in blue, and the outer area of the plates modeled with FEs in red.

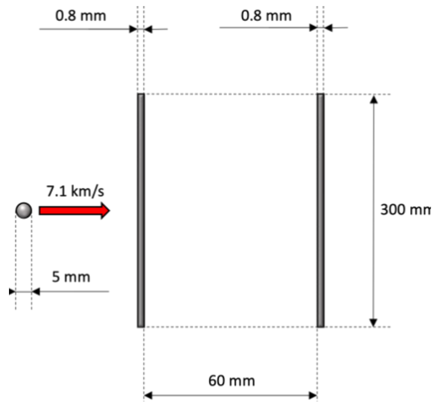

Figure 6: Whipple Shield target geometry.

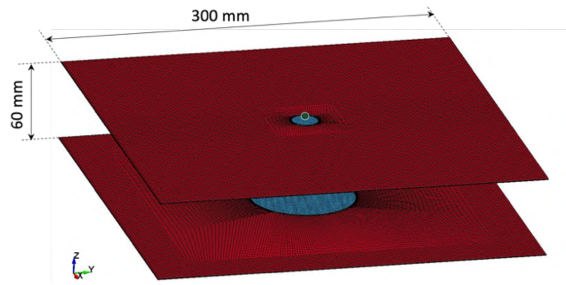

Figure 7: Whipple Shield simulation model.

To optimize computational efficiency, the size of the SPH domain related to the first plate was reduced compared to that related to the second plate. This decision was based on the logic of a Whipple shield, which allows for a larger impact area on the second plate. Indeed, the fragmentation of the projectile, which occurred on the impact with the first bumper, generates a debris cloud characterized by a dispersion angle with respect to the initial travel direction. This results in the kinetic energy being distributed over a larger area when it hits the second plate. The SPH domain size was determined by analyzing experimental data regarding the diameter of the crater formed on the second plate, allowing sufficient room for discrepancies between simulated and experimentally observed results. The diameter of the SPH domain of the first plate is 20 mm, while regarding the second plate, it was increased to 80 mm.

Due to a lack of values in scientific literature for the Johnson-Cook material model and Grüneisen EOS parameters for Al 2007, it was decided to use Al 2024-T3 aluminum alloy for the plates and the projectile. Indeed, as explained in the single plate simulation section, in HVIs the material's strength properties become negligible due to the immense pressures generated during impact, surpassing the material's strength limits, and the penetration capability is mostly ruled by the density of the projectile material [9]. Al 2024-T3 and Al 2007 not only have comparable densities, but they also show overall similar material properties. For the aforementioned reason, the Johnson-Cook model for Al 2024-T3 to represent the projectile instead of the Al 2007 model has been considered valid. Detailed input parameters for the elastic model, the Johnson-Cook model and the Grüneisen equation of state are provided in Tabs. 6, 7, and 8.

Material Property	Symbol	Value
Density	ρ	2.785 g/cm^3
Elastic Modulus	E	73.1 GPa
Poisson's Ratio	ν	0.33
Melting Temperature	T_m	775 K
Reference Temperature	T_0	294 K
Specific Heat	c_p	875 J/kgK

Table 6: Material properties of Al 2024-T3 aluminum alloy [18, 19].

Johnson-Cook parameters	Symbol	Value
Yield Stress	σ_y	369 MPa
Strain Hardening Param.	B	684 MPa
Strain Hardening Exp.	n	0.73
Strain Rate Param.	C	0.0083
Thermal Softening Exp.	m	1.7
Pressure Cut-off	σ_p	-1200 MPa
Damage Constant 1	D_1	0.13
Damage Constant 2	D_2	0.13
Damage Constant 3	D_3	- 1.5
Damage Constant 4	D_4	0.011
Damage Constant 5	D_5	0

Table 7: Johnson-Cook material model parameters for Al 2024-T3 aluminum alloy [18, 19].

Grüneisen parameters	Symbol	Value
EOS Constant 0	C	5240 m/s
EOS Constant 1	C_1	1.338
EOS Constant 2	C_2	0
EOS Constant 3	C_3	0
Grüneisen Parameter	Γ_0	2.00
Factor A	A	0.48

Table 8: Grüneisen EOS parameters for Al 2024-T3 aluminum alloy [18, 19].

Regarding the simulation validation, unlike the single plate test, the available data pertains only to the post-impact crater dimensions. In accordance with the simulation methodology, both craters display a circular shape, with their edges located far away from the hybrid coupling domain. Tab. 9 presents a comparative analysis of the diameter size of the craters and the corresponding relative errors.

	1st plate	2nd plate
Exp. Data	9.3 mm	58 mm
Simulation	9.9 mm	66.7 mm
Rel. Difference	6.5 %	14.97 %

Table 9: Crater diameter experimental results and relative differences in the Whipple shield HVI simulation.

By comparing the dimensions of the experimental and simulated craters and analyzing the relative differences, it is observed that the discrepancy in the rear plate is about twice the discrepancy observed in the bumper, which indicates that it is important to have a good match for the initial impact in the first plate in order to accurately predict the impact in the second plate.

Stress Analysis in the Plate

This section discusses the stress induced by HVI and its propagation from the impact region to the rest of the model. Both the first and second plates are analyzed, considering their differences and similarities.

In Figs. 8 and 9, the von Mises stresses detected on both the first (left column) and second (right column) plates are depicted. Key instants during the initial phase of the HVI phenomenon have been selected for representation, highlighting the moments before and after the debris cloud impacts the second plate.

The instant when the debris cloud impacts the second plate can be easily individuated. Indeed, the stress in the second plate is initially zero, but at about 7 μs the stress induced by the debris cloud impact becomes observable.

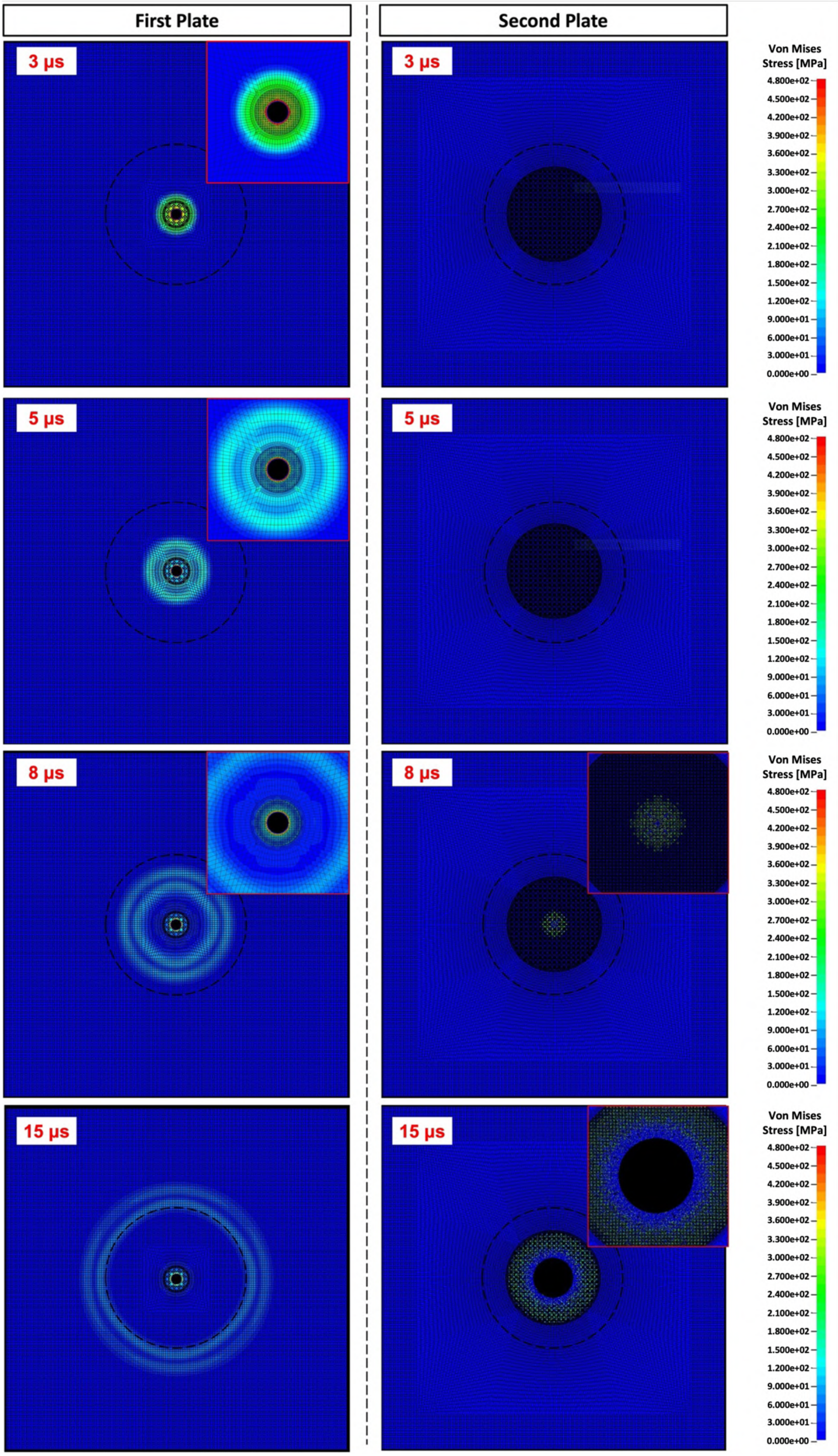

Figure 8: Von Mises Stress in Whipple shield HVI simulation (from 3 to 15 µs).

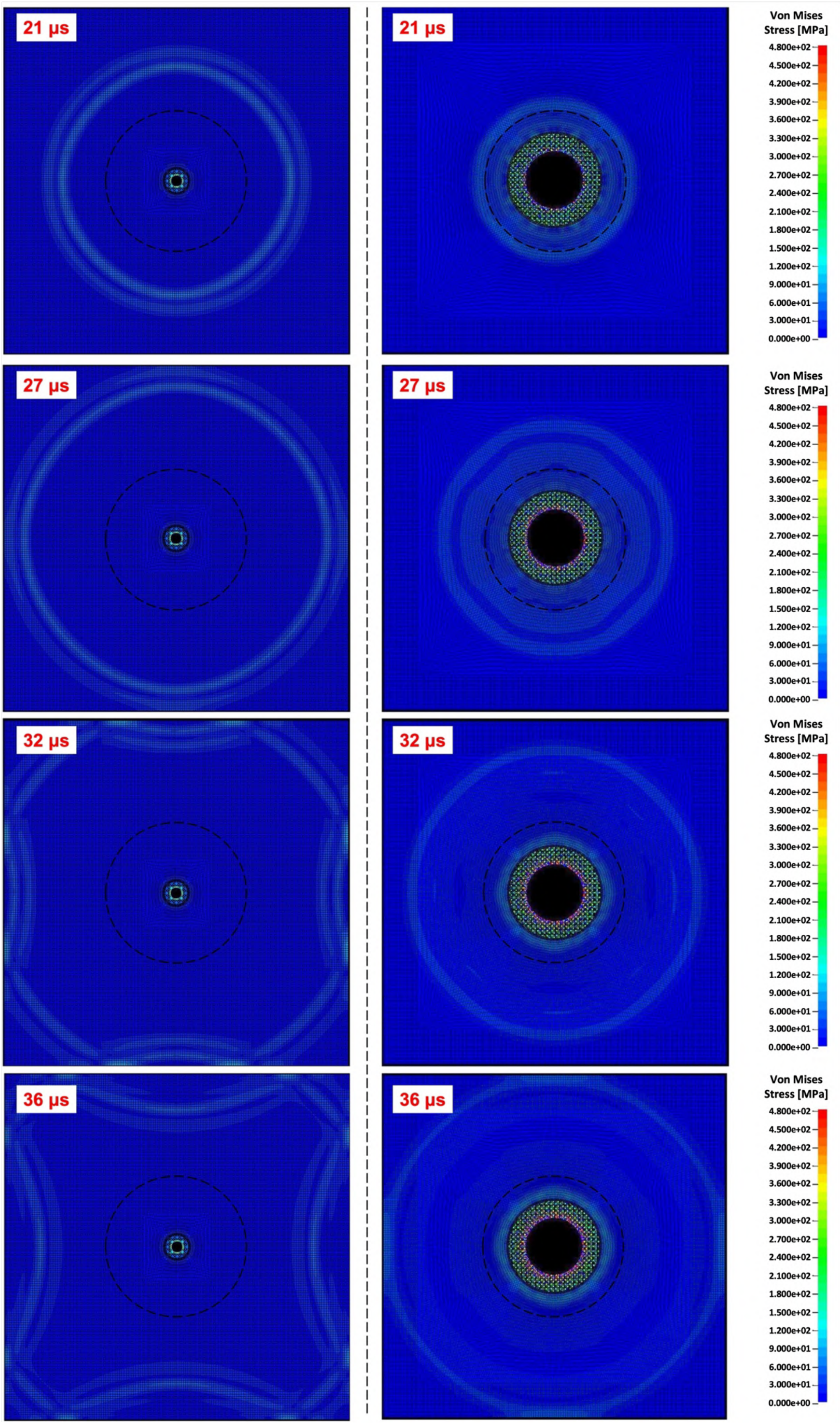

Figure 9: Von Mises Stress in Whipple shield HVI simulation (from 21 to 36 μs).

The findings suggest a distinct response of the two plates to the impact event, with the first plate exhibiting a more localized and transient stress distribution, whereas the second plate experiences a broader and lasting deformation. Since the first plate was the first to be involved in the impact phenomenon, the stress induced in the top plate reaches the edges more quickly and is mirrored on them. It is worth to note that in both the bumper and the second plate, the stress wave propagates independently of the direction, especially in the early stages of the phenomenon.

Further investigation of the temporal evolution and spatial distribution of the stresses could provide a comprehensive understanding of the response of the Whipple shield to HVI scenarios. Therefore, the von Mises stress values obtained at the same locations on both the first and second plates are examined. These points are located along a specific direction at various distances from the center of the plate on the first and second plates, respectively. They are located at 60, 95, and 130 mm from the center of the plate along the same axis.

This analysis makes it possible to study the propagation and attenuation of the stress wave along a given direction. To compare the structural behavior of the first plate with that of the second plate, the stress signals collected at different distances are juxtaposed in three different plots in Fig. 10. Each plot shows stress signals from equidistant points relative to both plates. The solid line refers to the bumper, while the dashed line is related to the second panel.

For both the bumper and the second plate, the curves follow a consistent pattern but experience a temporal shift proportional to the distance between data points and a gradual attenuation of signal amplitude as the observation point moves away from the impact area.

It is possible to highlight the different types of phenomena that hit the two plates during HVI. In the first plate, the stress profile is consistent with an impulsive shock-type excitation, characterized by a sudden high-amplitude spike. In the second plate, the signal still has a high amplitude, but it seems to be caused by an excitation that is prolonged in time.

In both cases, the stress waves travel through the surrounding structure at the same speed. To assess the speed of wave propagation, the time required for a stress peak to reach a subsequent data sampling point was measured and the distance between the two locations was taken. The results indicated a propagation velocity of 5.83 mm/µs, which is consistent with values documented in the published literature on the topic [20].

Comparing stress profiles can be challenging. However, it is crucial to highlight that stress peak levels are significantly higher in the first plate, and stress attenuation over distance occurs at a slower rate compared to the second plate. This comparative analysis is further elucidated in the Tab. 10.

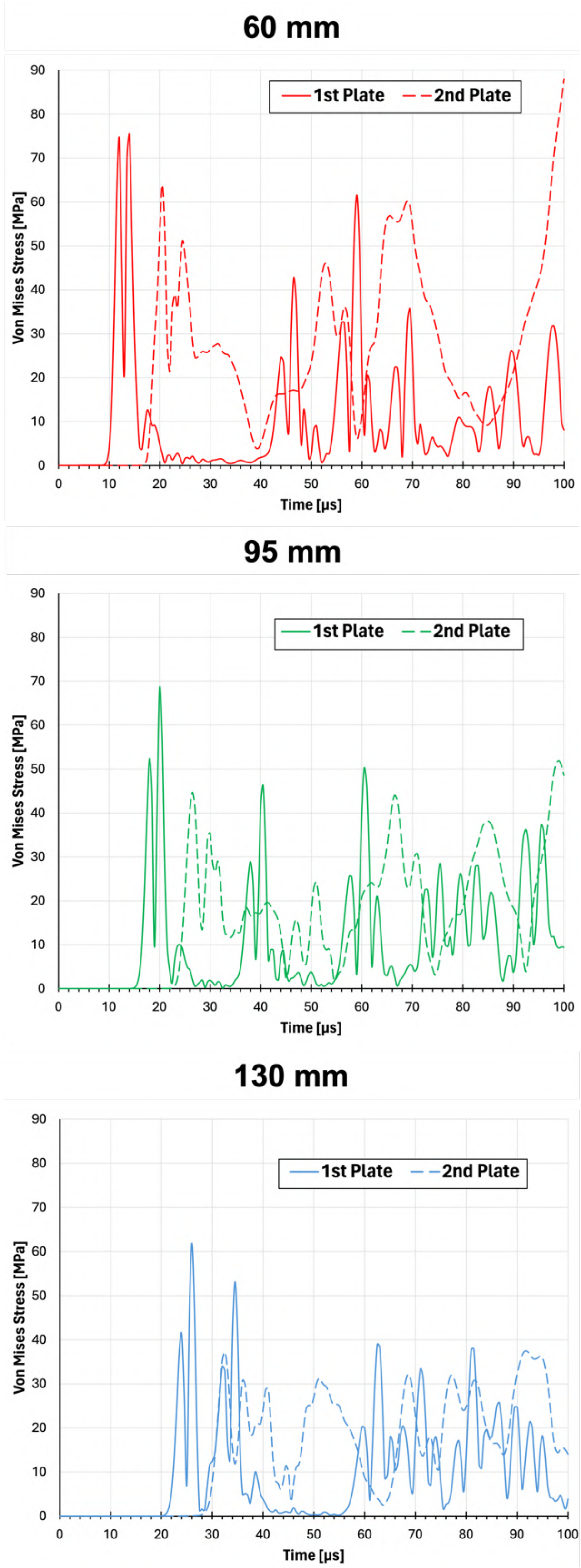

Figure 10: Von Mises Stress plot comparison in 1st and 2nd plate.

In the first plate, the highest peak experiences a gradual reduction of 7.94% when comparing the maximum value recorded at a distance of 60 mm from the center with that recorded at 95 mm. Conversely, in the second plate, the highest peak undergoes a reduction of approximately 30%. Similarly, transitioning from 95 mm to 130 mm, a reduction of 9.5% is observed in the first plate, while in the second plate, a reduction of approximately 20% is evident.

	Max Von Mises stress at 60 mm	**Max Von Mises stress at 95 mm**	**Max Von Mises stress at 130 mm**
1st plate	75.3 MPa	68.4 MPa	61.9 MPa
% red.	/	- 7.94 %	- 9.50 %
2nd plate	63.9 MPa	44.7 MPa	37.2 MPa
% red.	/	- 30.0 %	- 20.2 %

Table 10: Von Mises Stress plot comparison in 1st and 2nd plate.

SUMMARY

Having identified the limitations associated with experimental testing (i.e., high cost, maximum achievable impact velocity and minimum projectile dimensions), the main numerical modelling techniques for HVIs, including the FEM and SPH, were evaluated. The advantages and limitations of both techniques were highlighted, and the possibility of developing hybrid models that combine both methodologies was considered. Such coupling could be achieved implementing an interface between a domain modelled by SPH and another modelled by FEs.

A study of the effects of a HVI on a single-plate system oriented perpendicular to the velocity direction of the projectile was carried out. A comparative analysis was performed to identify the optimal settings for the contact methodology between FEM and SPH zones and the shape of the SPH domain. The results were compared with experimental data for model validation. The study evaluated the mutual influence of these parameters not only on post-impact geometric parameters such as crater diameter, dimensions, and debris cloud propagation velocity, but also on effects related to the uniformity of the stress field induced by HVI. It was found that a configuration with a circular SPH domain connected to the surrounding FEM zone by hybrid elements gives the best results both in terms of post-impact geometric parameters (with the smallest overall discrepancy of 4.06%) and in terms of uniformity of stress propagation in the area surrounding the impact.

A comprehensive analysis of a HVI on a Whipple shield was then performed. The implemented model, based on the results of previous comparative analyses,. The study showed the effectiveness of the Whipple shield in fragmenting and slowing down the projectile, thus dissipating its kinetic energy. An analysis of the propagation of stress waves induced by the HVI was performed. The study demonstrated that the higher stress levels are primarily transmitted through the bumper to the rest of the satellite structure.

NEXT STEPS

Despite the limitation of the size of the FEM domain surrounding the SPH impact zone, it is possible to extend the developed methodology to more complex geometries, allowing the assessment of the effects of a HVI on a real satellite and the development of vulnerability maps for the analyzed space platform.

The results indicate significant opportunities for developing a coupled SPH/FEM modeling methodology to analyze HVIs on space structures. However, challenges and areas of development still accompany the path towards a more comprehensive application of this methodology.

One of the main barriers identified is the need for experimental data to further validate the numerical approach. It is necessary to investigate the methodology's applicability to materials with more complex mechanical characteristics, such as composite materials, ceramics, fabrics, and metal foams, used in space subsystems like solar panels or deployable and inflatable structures. This study would improve our understanding of real structures' behavior and make it possible to adapt the methodology, accordingly, further enhancing its applicability and effectiveness in the space context.

ACKNOWLEDGMENT

The authors would like to express their gratitude to Airbus Defence and Space for providing the data used for the validation of the simulation on the Whipple Shield.

REFERENCES

1. European Space Agency, ESA (2024) Annual Space Environment REPORT.
2. Kessler, D.J. & Cour-Palais, B.G. (1978). Collision frequency of artificial satellites: The creation of a debris belt. *J. Geophys. Res. Space Phys*. **83**(A6), 2637-2646.
3. Whipple, F.L. (1947). Meteorites and space travel. *Astron. J.*, 52, 131.
4. Wen, K., Chen, X.W. & Lu, Y.G. (2021). Research and development on hypervelocity impact protection using Whipple shield: An overview. *Def. Technol.*, **17**(6), 1864-1886.
5. Pavarin, D., Francesconi, A., Destefanis, R., Lambert, M., Bettella, A., Debei, S. & Angrilli, F. (2006). Acceleration fields induced by hypervelocity impacts on spacecraft structures. *Int. J. Impact Eng.*, **33**(1-12), 580-591.
6. Ryan, S. (2009). Numerical simulation in micrometeoroid and orbital debris risk assessment. In *Predictive Modeling of Dynamic Processes* (Eds. S. Hiermaier), Springer US, Boston, MA, pp417-446.

7. He, Q.G., Chen, X. & Chen, J.F. (2020). Finite element-smoothed particle hydrodynamics adaptive method in simulating debris cloud. *Acta Astronaut.*, 175, 99-117.
8. Sibeaud, J.M., Héreil, P.L. & Albouys, V. (2003). Hypervelocity impact on spaced target structures: Experimental and Ouranos simulation achievements. *Int. J. Impact Eng.*, **29**(1-10), 647-658.
9. Clough, N., Lieblein, S. & McMillan, A.R. (1969). *Crater characteristics of 11 metal alloys under hyper-velocity impact including effects of projectile density and target temperature.* National Aeronautics and Space Administration.
10. ASM Handbook (1990). *Properties and selection: nonferrous alloys and special-purpose materials*.
11. Johnson, G.R. & Holmquist, T.J. (1989). *Test data and computational strength and fracture model constants for 23 materials subjected to large strains, high strain rates, and high temperatures*. Los Alamos National Laboratory, Los Alamos, NM, Report No. LA-11463-MS.
12. Spear, D.G., Palazotto, A.N. & Kemnitz, R.A. (2021). Modeling and simulation techniques used in high strain rate projectile impact. *Mathematics*, **9**(3), 274.
13. Legaud, T., Le Garrec, M., Van Dorsselaer, N. & Lapoujadet, V. (2019). Improvement of satellites shielding under high velocity impact using advanced SPH method. In *Proc. 12th European LS-DYNA Conf.* DYNAmore GmbH, Stuttgart, Germany.
14. Lacome, J.L., Espinosa, C. & Gallet, C. (2002). Simulation of hypervelocity spacecrafts and orbital debris collisions using smoothed particle hydrodynamics in LS-DYNA. In *Proc. 5th Dynamics and Control of Systems and Structures in Space Conference*.
15. Harazim, M. (2023). *Hypervelocity Impact Simulation using Smoothed-Particle Hydrodynamics* [Master's thesis, Delft University of Technology]. TU Delft Repository.
16. Hallquist, J.O. (2006). LS-DYNA theory manual. Livermore software Technology corporation.
17. Tech. rep. (1997) "Columbus Meteoroid and Debris Protection Shield (MOPS)", Phase II Study Extension, Work Package 1440 "Impact Test Performance", ESTEC Contract 8732190, Final Report.
18. Buyuk, M., Kan, S. & Loikkanen, M.J. (2009). Explicit finite-element analysis of 2024-T3/T351 aluminium material under impact loading for airplane engine containment and fragment shielding. *J. Aerosp. Eng.*, **22**(3), 287-295
19. Lesuer, D.R. (2000). Experimental investigations of material models for Ti-6Al-4V titanium and 2024-T3 aluminum. Report No. DOT/FAA/R-00/25, Final Report.
20. Esfarjani, S. M. (2019). Evaluation of effect changing temperature on lamb-wave based structural health monitoring. *J. Mech. Energy Eng.*, **3**(4), 329-336.